

# Mass and energy balance calculations for an artificial ice reservoir (Icestupa)

Suryanarayanan Balasubramanian<sup>1,\*</sup>, Martin Hoelzle<sup>1</sup>, Michael Lehning<sup>2</sup>,

Sonam Wangchuk<sup>3</sup>, Johannes Oerlemans<sup>4</sup> and Felix Keller<sup>5</sup>

<sup>1</sup> University of Fribourg, Fribourg, Switzerland

<sup>2</sup> WSL Institute for Snow and Avalanche Research, Davos, Switzerland

<sup>3</sup> Himalayan Institute of Alternatives Ladakh, Leh, India

<sup>4</sup> Institute for Marine and Atmospheric Research, Utrecht University, Utrecht, The Netherlands

<sup>5</sup> Academia Engiadina, Samedan, Switzerland

Correspondence\*:

Suryanarayanan Balasubramanian

suryanarayanan.balasubramanian@unifr.ch

## 2 ABSTRACT

Artificial Ice Reservoirs (AIRs) can successfully store water during winter and release the water during spring and summer. This makes them a reliable fresh water resource for irrigation in dry environments. Several AIRs have been built but studies of their water storage capacity and efficiency are scarce. This study models a cone-shaped AIR popularly called Icestupa. Processes involved in the development and temporal evolution of an Icestupa are calculated by a physically-based model using equations governing the heat transfer, vapour diffusion and transport of water that undergoes phase changes. These processes were quantified using meteorological data in conjunction with fountain spray information (mass input of an Icestupa) to estimate the quantity of frozen, melted, evaporated and runoff water at a location called 'Eispalast' in Fribourg, Switzerland. At this measurement site, an Icestupa was built for model validation purposes. The model was further tested by performing a sensitivity and uncertainty study showing that the most sensitive parameters are the ice emissivity and the temperature threshold used to determine precipitation phase. Model calculations estimate that the Eispalast Icestupa stored about 6% of the total water sprayed as ice. In addition, we found that reducing nozzle diameter of the fountain from 5 mm to 3 mm increases the water storage up to 78% without compromising on the storage duration.

Keywords: ictestupa, mass balance, water storage, climate change adaptation, geoengineering

## 1 INTRODUCTION

Seasonal snow cover, glaciers and permafrost are expected to change their water storage capacity due to climate change with major consequences for downriver water supply (Immerzeel et al., 2019). The challenges brought about by these changes are especially important for dry mountain environments such as in Central Asia or the Andes, which directly rely on the seasonal meltwater for their farming and drinking needs (Hoelzle et al., 2019; Apel et al., 2018; Buytaert et al., 2017; Chen et al., 2016; Unger-Shayesteh



**Figure 1.** Icestupa in Ladakh, India on March 2017 was 24 m tall and contained around 3700  $m^3$  of water. Picture Credits: Lobzang Dadul

25 et al., 2013). Some villages in Ladakh, India have already been forced to relocate due to glacial retreat and  
26 the corresponding loss of their main fresh water resources (Grossman, 2015).

27 Artificial ice reservoirs (AIRs) have been considered to be a feasible way to adapt to these changes (Hock  
28 et al., 2019; Nüsser et al., 2019b). An AIR is a human-made ice structure typically constructed during the  
29 cold winter months and designed to slowly release freshwater during the warm and dry spring and summer  
30 months. The main purpose of AIRs is irrigation. Therefore, AIRs are designed to store water in the form of  
31 ice as long into the summer as possible. The energy required to construct an AIR is usually derived from  
32 the gravitational head of the source water body. Some are constructed horizontally by freezing water using  
33 a series of checkdams and others are built vertically by spraying water through fountain systems (Nüsser  
34 et al., 2019a). The latter are colloquially referred to as Icestupas and are the subject of this study.

35 A typical Icestupa just requires a pipeline attached to a vertically mounted metal pipe with a fountain  
36 nozzle for construction. Their water source is usually a high altitude lake or glacial stream. Due to the  
37 altitude difference between the pipeline input and fountain output, water ejects from the fountain nozzle as  
38 droplets that eventually lose their latent heat to the atmosphere and accumulate as ice around the metal pipe.  
39 The fountain nozzle is raised through addition of further pipes as and when significant ice accumulates.  
40 Typically, a dome of branches is constructed around the metal pipe so that such pipe extensions can be  
41 done from within this dome. During the winter, the fountain is manually activated from sunset to sunrise.  
42 Threads, tree branches and fishing nets are used to guide and accelerate the ice formation.

43 Since their invention in 2013 (Wangchuk, 2014), Icestupas have gained widespread publicity in the region  
44 of Ladakh, Northern India since they require very little infrastructure, skills and energy to be constructed  
45 in comparison to other water storage technologies. Compared to other AIR geometries, Icestupas (Fig.  
46 1) can be built at lower altitudes and last much longer into the summer than other types of ice structures  
47 (Wangchuk, 2014). However, to date, no reliable estimates exist about the amount of sprayed water that  
48 is necessary to create them and the meltwater they provide (Nüsser et al., 2019a). Rough estimates of  
49 Icestupa meltwater in Ladakh suggest that the water loss during the construction process is considerable  
50 (see Appendix 8.1). A complete set of measurements of the water storage and energy balance are required  
51 to understand the cause of the water losses better and increase the construction efficiency.

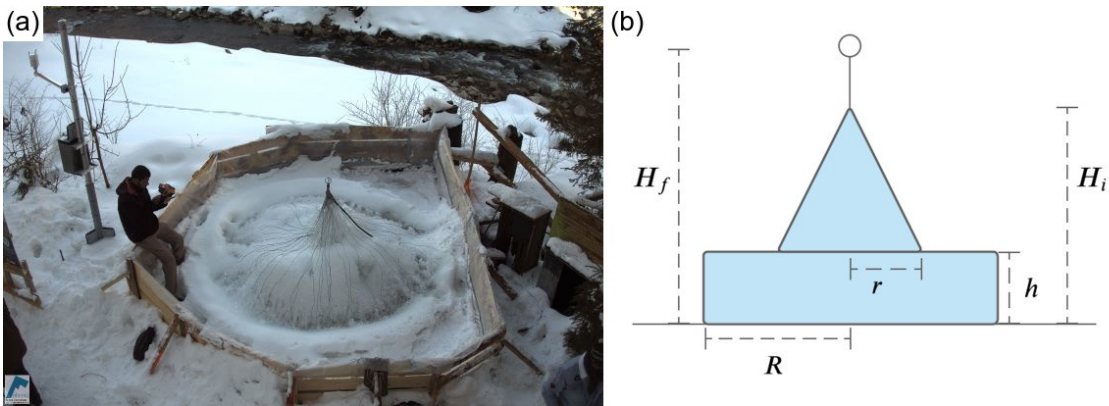


**Figure 2.** (a) The ice structure during the first validation measurement as seen on the webcam image of 14<sup>th</sup> Feb. (b) The corresponding cross section of the EP ice structure with the field estimates of  $r$ ,  $R$ ,  $h$ ,  $H_i$ ,  $H_f$  used to determine the Icestupa volume is shown on the right.

52 In this paper, we aim to develop a physically-based model of a vertical AIR (or Icestupa) that can quantify  
 53 their storage efficiency using existing weather and water usage information. Mass and energy balance  
 54 equations were used to estimate the quantity of water frozen, melted, evaporated and runoff. Sensitivity  
 55 and uncertainty analysis were performed to identify the most critical parameters and the variance caused  
 56 by them. For validation, we created an Icestupa at an accessible site (called Eispalast) near Schwarzsee  
 57 close to the city of Fribourg, Switzerland, allowing easy maintenance and control of the measurements.  
 58 Due to the low altitude of the site with relatively high winter temperatures, only a small Icestupa could  
 59 be established during winter 2018/19 to provide us with model validation data. Our model and validation  
 60 experiments provide first steps towards evaluating the effectiveness of a vertical AIR for irrigation and  
 61 allow us to outline some preliminary guidelines for consideration when a construction of an Icestupa for  
 62 water storage is envisaged.

## 2 STUDY SITE

63 The Eispalast (EP) site in the Schwarzsee region lies at 967 m a.s.l.. In the winter (Oct-Apr), mean daily  
 64 maximum and minimum air temperatures vary between -4 and 14 °C. Clear skies are rare, averaging  
 65 around 7 days, and precipitation amounts average 155 mm per month during winter (Meteoblue, 2020).  
 66 The site was situated adjacent to a stream resulting in high humidity values across the study period. Within  
 67 the EP site, an enclosure with a 1.8 m radius was constructed for the experiment. An automatic weather  
 68 station (AWS) was adjacent to the wooden boundary as shown in Fig. 2. The fountain used for spraying  
 69 water had a nozzle diameter of 5 mm and a height of 1.35 m, and was placed in the centre of the wooden  
 70 enclosure. The water was transferred from a spring water source at 1267 m a.s.l. by pipeline and flowed  
 71 via a flowmeter and an air escape valve to the nozzle, where it was sprinkled with a spray radius of around  
 72 1.7 m. The air escape valve was installed to avoid errors in the flow measurements due to air bubbles. In  
 73 addition, a webcam guaranteed a continuous survey of the site during the construction of the Icestupa.

### 74 2.1 Construction

75 From 30<sup>th</sup> January to 18<sup>th</sup> March 2019 the Icestupa was constructed through the fountain spray, which  
 76 was manually switched on if measured air temperature was below -5 °C after sunset and was switched  
 77 off as soon as the ice was exposed to daylight or temperatures were above 0 °C. The water spray of the  
 78 fountain was initially adjusted so that most of the water droplets land within the wooden boundary zone.  
 79 The ice formation was guided by adding a metal framework at the ice structure base after the first night of

80 operation. Several cotton threads were tied between the ice structure base and fountain pole for accelerating  
 81 and further guiding the ice formation process.

## 82 2.2 Measurements and Data

83 Measurements comprising air temperature, relative humidity, water flow rate, wind speed and direction  
 84 were made every 5 minutes throughout the construction period. The water flow rate or discharge was  
 85 measured via an ultrasonic sensor attached to the fountain supply pipeline. Precipitation data was derived  
 86 from the Plaffeien AWS (IDAWEB, 2019) located 8.8 km away from the measurement site at an altitude of  
 87 1042 m a.s.l.

88 In addition, we used ERA5 reanalysis dataset (Copernicus Climate Change Service (C3S), 2017) for  
 89 filling data gaps and adding data that were not measured directly at the EP site. We recognised during  
 90 our data analysis that, except precipitation, all the other meteorological variables of the EP site correlated  
 91 much better with the ERA5 dataset than the nearby Plaffeien AWS dataset. The 2 m temperature parameter  
 92 correlated with air temperature ( $r^2 = 0.9$ ), surface pressure parameter correlated with air pressure ( $r^2 = 1$ )  
 93 and 10m wind speed parameter (derived from horizontal and vertical components) correlated with wind  
 94 speed ( $r^2 = 0.6$ ). The ERA5 reanalysis dataset has a good correlation with lower elevation sites in  
 95 Switzerland (Scherrer, 2020). The hourly ERA5 data and the 10 minute Plaffeien AWS data were linearly  
 96 interpolated to the 5 minute data frequency of the EP AWS.

97 Due to a power failure, all data from the EP AWS was lost from 27<sup>th</sup> February 15:20 2019 to 2<sup>nd</sup> March  
 98 15:00 2019 (equivalent to around 7% of the measurement period). During heavy snowfall events, the  
 99 ultrasonic wind sensor was blocked and recorded zero values. ERA5 was used to fill such errors and data  
 100 gaps. Near-surface humidity is not provided directly in ERA5 dataset, but from near-surface (2 m from the  
 101 surface) temperature ( $T_{ERA5}$ ) and dew point temperature ( $Tw_{ERA5}$ ) the relative humidity (RH) at 2 m  
 102 was calculated as:

$$RH = 100 \cdot \frac{e_{sat}(Tw_{ERA5})}{e_{sat}(T_{ERA5})} \quad (1)$$

103 where the saturation vapour pressure function  $e_{sat}$  is expressed with the Teten's formula (Tetens, 1930):

$$e_{sat}(T) = a_1 \cdot e^{(a_3 \cdot \frac{T}{(T+273.16-a_4)})} \quad (2)$$

104 with T in °C and the parameters set for saturation over water ( $a_1 = 611.21$  Pa,  $a_3 = 17.502$  and  $a_4 = 32.19$   
 105 K) according to Buck (1981). Zero wind speed values were recorded whenever snow accumulated on the  
 106 ultrasonic wind sensor. All such null values were replaced using the ERA5 dataset.

107 The ERA5 grid point chosen (Latitude 46° 38' 24" N, Longitude 7° 14' 24" E) for the EP site was around  
 108 9 km away from the actual site. All the ERA5 variables were therefore fitted with the EP dataset via linear  
 109 regressions. With the modified ERA5 dataset, we were also able to further extend the EP dataset and allow  
 110 the model to run beyond 18<sup>th</sup> March 2019. Precipitation was filled as null values beyond 18<sup>th</sup> March 2019.

111 2.2.1 Field Measurements for Validation  
 112 The volume was determined by decomposing the ice structure into a cylinder (length  $2R$  and height  $h$ )  
 113 and a cone (radius  $r$  and height  $(H_i - h)$ ) through the following equation:

$$V = \pi \cdot R^2 \cdot h + 1/3 \cdot \pi \cdot r^2 \cdot (H_i - h) \quad (3)$$

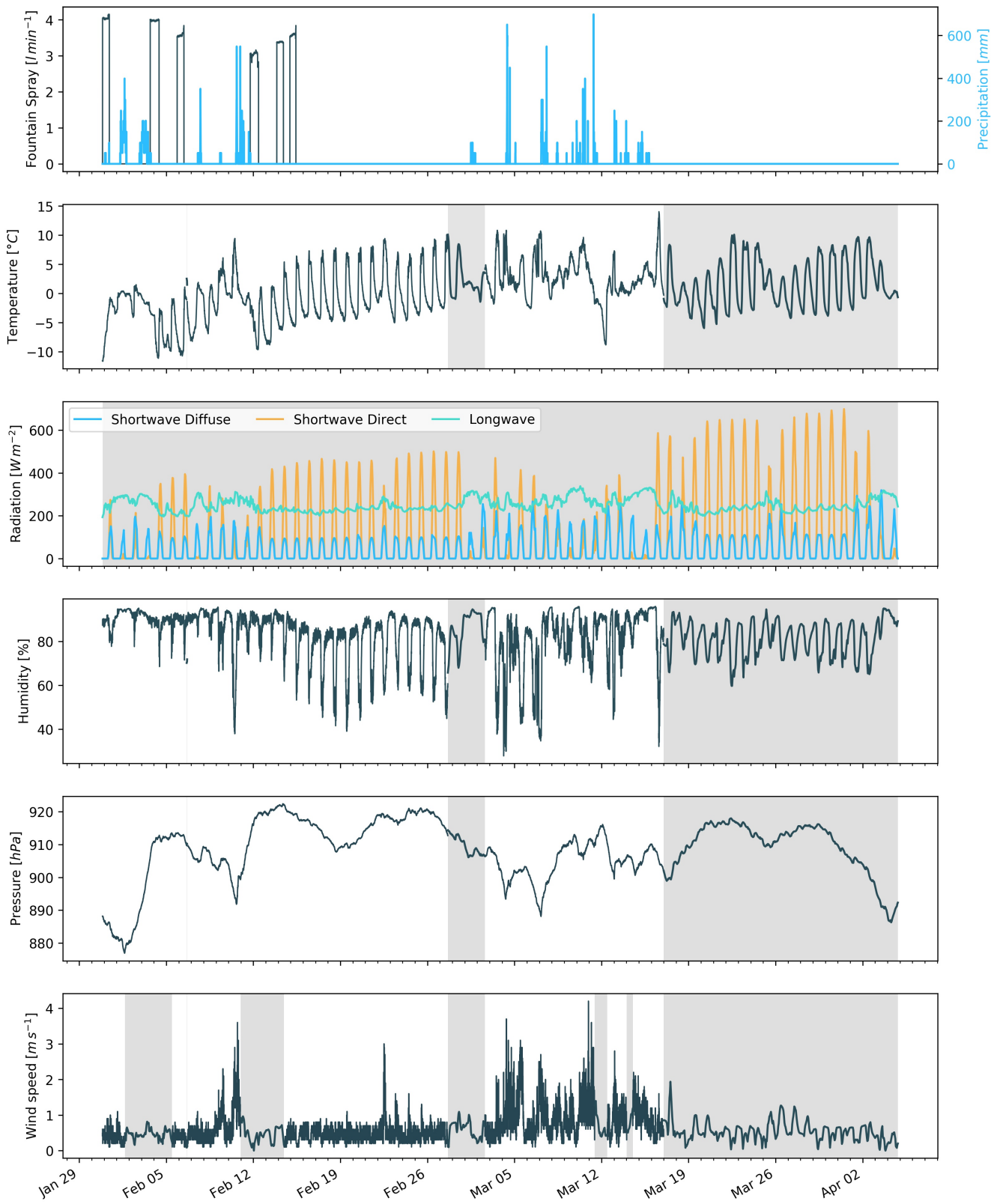


**Figure 3.** Measurements at the AWS of EP were used as main model input data in 5 minute frequency. Plaffeien AWS provided the precipitation data. Incoming shortwave and longwave radiation were obtained from ERA5 reanalysis dataset. Several data gaps and errors were also filled from the ERA5 dataset (shaded regions).

114 Manual measurements were performed at the end of the freezing period on 14<sup>th</sup> February 16:00 2019  
 115 (only one more fountain run was possible after this date) to estimate  $r, R, h, H_i, H_f$  (see Fig. 2 for the  
 116 different geometry components):

$$0.55 \leq r \leq 1m ; 1.1 \leq R \leq 1.2m ; 0.1 \leq h \leq 0.2m ; 0.6 \leq H_i \leq 0.8m ; 1.3 \leq H_f \leq 1.4m$$

117 The ranges of the variables show the variance of the Icestupa's dimensions across different compass  
 118 orientations. Correspondingly, the volume range estimated for the first validation point was  $0.857 \pm 0.186$   
 119  $m^3$  on 14<sup>th</sup> February 16:00 2019.

120 The second validation point corresponds to the end of the melting process on 10<sup>th</sup> March 18:00 2019.  
 121 Based on the webcam imagery and manual measurement, a thin layer of ice with an observed thickness  
 122 between 0.01 to 0.06 m could be quantified. This results in the volume range for the second validation to  
 123 be  $0.13 \pm 0.09 m^3$  on 11<sup>th</sup> March 2019

124 In reality, the EP ice structure was more cylindrical until a height of 0.2 m and conical afterwards until a  
 125 height of 0.6 m with a radius of 1.18 m. However, we assume a conical shape of this ice structure in order  
 126 to apply the modelling strategy described below.

### 3 MODEL SETUP

127 The model consists of three parts which calculate, a) the geometric evolution of the Icestupa, b) the energy  
 128 balance and c) the mass balance as shown schematically in Fig. 4. A bulk energy and mass balance model  
 129 is used to calculate the amounts of ice, meltwater, water vapour and runoff water of the Icestupa every 5  
 130 minutes.

#### 3.1 Icestupa geometric evolution

131 Radius  $r_{ice}^i$  and height  $h_{ice}^i$  define the dimensions of the Icestupa assuming its geometry to be a cone as  
 132 shown in Fig. 5. The surface area  $A^i$  exposed to the atmosphere and volume  $V^i$  are:

$$A = \pi \cdot r_{ice} \cdot \sqrt{r_{ice}^2 + h_{ice}^2} \quad (4)$$

$$V = \pi/3 \cdot r_{ice}^2 \cdot h_{ice} \quad (5)$$

134 Note that we do not specify the time step superscript  $i$  of the shape variables  $A, V, r_{ice}$  and  $h_{ice}$  for  
 135 brevity. The equations used henceforth display model time step superscript  $i$  only if it is different from the  
 136 current time step.

137 With the mass of the Icestupa  $M_{ice}$ , its current volume can also be expressed as:

$$V = M_{ice}/\rho_{ice} \quad (6)$$

138 where  $\rho_{ice}$  is the density of ice ( $917 kg m^{-3}$ ). The model of the Icestupa is initialised with a thickness  
 139 of  $\Delta x$  (defined in 3.2) and a circular area of radius  $r_F$ . The constant  $r_F$  represents the mean spray radius  
 140 of the fountain. This fountain spray radius is determined by modelling the projectile motion of the water

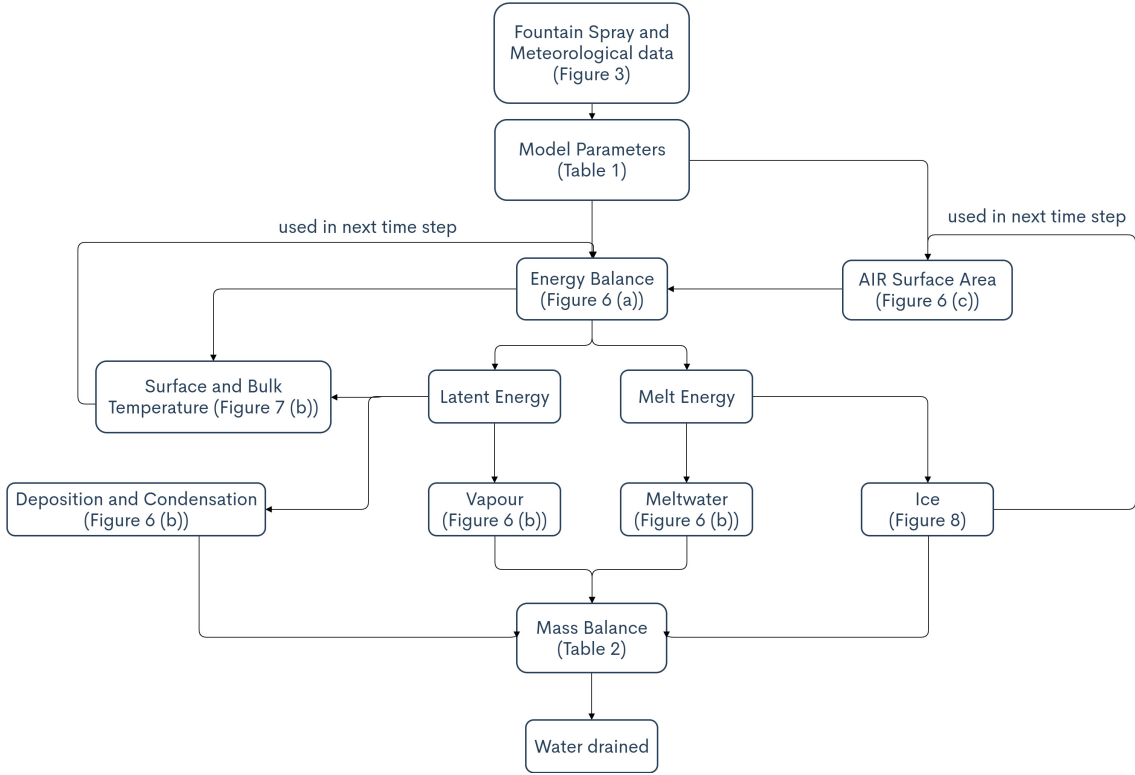


**Figure 4.** Model schematic showing the algorithm used in the model at every time step. Further details about the variables can be found in the associated tables and figures.

141 droplets. Using mass conservation, the droplet speed  $v_F$  can be determined from the spray rate  $d_F$  and the  
 142 diameter  $dia_F$  of the nozzle as follows:

$$v_F = \frac{d_F}{\pi \cdot dia_F^2 / 4} \quad (7)$$

143 Afterwards, we assume that the water droplets move with an air friction free projectile motion from  
 144 the fountain nozzle with a height  $h_F$  to the ice/ground surface. The resulting spray radius  $r_F$  was then  
 145 determined from the projectile motion equation as follows:

$$r_F = \frac{v_F \cdot \cos\theta_F (v_F \cdot \sin\theta_F + \sqrt{(v_F \cdot \sin\theta_F)^2 + 2 \cdot g \cdot h_F})}{g} \quad (8)$$

146 where  $g = 9.8 \text{ ms}^{-2}$  is the acceleration due to gravity and  $\theta_F = 45^\circ$  is the angle of launch.

147 During subsequent time steps, the dimensions of the Icestupa evolve assuming a uniform ice formation  
 148 and decay across its surface area with an invariant slope  $s_{cone} = \frac{h_{ice}}{r_{ice}}$  as shown in Fig. 5. During these time  
 149 steps, the volume is parameterised using Eqn. 5 as:

$$V = \pi / 3 \cdot r_{ice}^3 \cdot s_{cone} \quad (9)$$

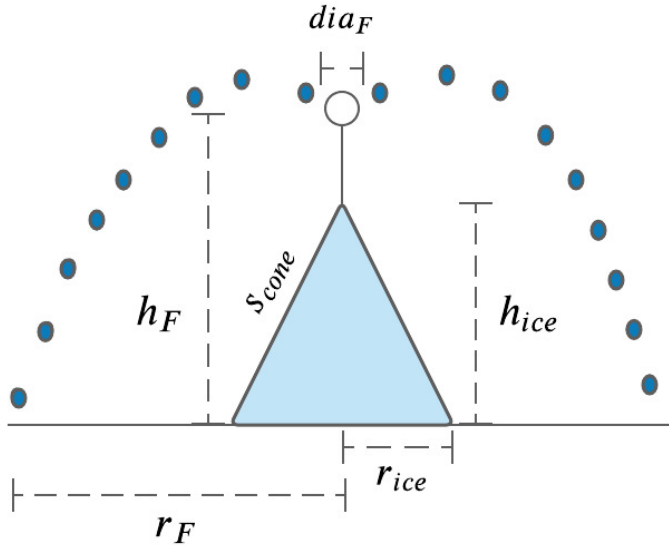


**Figure 5.** Shape variables and fountain constants of the EP Icestupa.  $r_{ice}$  is the radius,  $h_{ice}$  is the height and  $s_{cone}$  is the slope of the ice cone.  $r_F$  is the spray radius,  $h_F$  is the height and  $dia_F$  is the nozzle diameter of the fountain.

150 However, the Icestupa cannot outgrow the maximum range of the water droplets ( $(r_{ice})_{max} = r_F$ ).  
 151 Combining equations 5, 6 and 9, the geometric evolution of the Icestupa at each time step  $i$  can be  
 152 determined by considering the following rules:

$$(r_{ice}, h_{ice}) = \begin{cases} (r_F, \Delta x) & \text{if } i = 0 \\ (r_{ice}^{i-1}, \frac{3 \cdot M_{ice}}{\pi \cdot \rho_{ice} \cdot (r_{ice}^{i-1})^2}) & \text{if } r_{ice}^{i-1} \geq r_F \text{ and } \Delta M_{ice} > 0 \text{ where } \Delta M_{ice} = M_{ice}^{i-1} - M_{ice}^{i-2} \\ (\frac{3 \cdot M_{ice}}{\pi \cdot \rho_{ice} \cdot s_{cone}})^{1/3} \cdot (1, s_{cone}) & \text{otherwise} \end{cases} \quad (10)$$

### 153 3.2 Energy Balance

154 The energy balance equation (Hock, 2005) for the Icestupa is formulated as follows:

$$q_{net} = q_{SW} + q_{LW} + q_L + q_S + q_F + q_G \quad (11)$$

155 where  $q_{net}$  is the net energy flux in  $[W m^{-2}]$ ;  $q_{SW}$  is the net shortwave radiation;  $q_{LW}$  is the net longwave  
 156 radiation;  $q_L$  and  $q_S$  are the turbulent latent and sensible heat fluxes.  $q_F$  represents the heat exchange of the  
 157 fountain water droplets with the AIR ice surface during fountain on time steps.  $q_G$  represents ground heat  
 158 flux between Icestupa surface and Icestupa interior. Energy transferred in the direction of the ice surface is  
 159 always denoted as positive and away as negative.

160 Equation 11 is usually referred to as the energy budget for “the surface”, but practically it must apply to a  
 161 surface layer of ice with a finite thickness  $\Delta x$ . The energy flux acts upon the Icestupa surface layer which  
 162 has an upper and a lower boundary defined by the atmosphere and the ice body of the Icestupa, respectively.  
 163 The parameter selection for  $\Delta x$  is based on the following two arguments: (a) the ice thickness  $\Delta x$  should

164 be small enough to represent the daily surface temperature variations and (b)  $\Delta x$  should be large enough  
 165 for these temperature variations to not reach the bottom of the surface layer. Therefore, we introduced a 5  
 166 mm thick ice surface layer, over which the energy balance is calculated. A sensitivity analysis was later  
 167 performed to understand the influence of this factor. Here, we define the surface temperature  $T_{ice}$  to be  
 168 the modelled average temperature of the Icestupa surface layer and the energy flux  $q_{net}$  is assumed to act  
 169 uniformly across the Icestupa area  $A$ .

### 170 3.2.1 Net Shortwave Radiation $q_{SW}$

171 The net shortwave radiation  $q_{SW}$  is computed as follows:

$$q_{SW} = (1 - \alpha) \cdot (SW_{direct} \cdot f_{cone} + SW_{diffuse}) \quad (12)$$

172 where  $SW_{direct}$  and  $SW_{diffuse}$  are the ERA5 direct and diffuse short wave radiation,  $\alpha$  is the modelled  
 173 albedo and  $f_{cone}$  is the area fraction of the ice structure exposed to the direct shortwave radiation.

174 We model the albedo using a scheme described in Oerlemans and Knap (1998). The scheme records the  
 175 decay of albedo with time after fresh snow is deposited on the surface.  $\delta t$  records the number of time steps  
 176 after the last snowfall event. After snowfall, albedo changes over a time step,  $\delta t$ , as

$$\alpha = \alpha_{ice} + (\alpha_{snow} - \alpha_{ice}) \cdot e^{(-\delta t)/\tau} \quad (13)$$

177 where  $\alpha_{ice}$  is the bare ice albedo value (0.35),  $\alpha_{snow}$  is the snow ice albedo value (0.85) and  $\tau$  is a decay  
 178 rate, which determines how fast the albedo of the ageing snow reaches this value. The decay rate  $\tau$  is  
 179 assumed to have a base value of 10 days similar to values obtained by Schmidt et al. (2017) for wet surfaces  
 180 and its maximal value is set based on observations by Oerlemans and Knap (1998) as shown in Table 1.  
 181 Furthermore, the albedo  $\alpha$  varies depending on the water source that formed the current Icestupa surface.  
 182 Correspondingly, the albedo is reset to the value of bare ice albedo if the fountain is spraying water onto  
 183 the current ice surface and to the value of fresh snow albedo if a snowfall event occurred. Snowfall events  
 184 are assumed if the air temperature is below  $T_{ppt} = 1^{\circ}C$  (Fujita and Ageta, 2000).

185 The area fraction  $f_{cone}$  of the ice structure exposed to the direct shortwave radiation depends on the  
 186 shape considered. The direct solar radiation incident on the AIR surface is first decomposed into horizontal  
 187 and vertical components using the solar elevation angle  $\theta_{sun}$ . For a conical shape, half of the total curved  
 188 surface is exposed to the vertical component of the direct shortwave radiation and the projected triangle  
 189 of the curved surface is exposed to the horizontal component of the direct shortwave radiation. The solar  
 190 elevation angle  $\theta_{sun}$  used is modelled using the parametrisation proposed by Woolf (1968). Accordingly,  
 191  $f_{cone}$  is determined as follows:

$$f_{cone} = \frac{(0.5 \cdot r_{ice} \cdot h_{ice}) \cdot \cos\theta_{sun} + (\pi \cdot r_{ice}^2 / 2) \cdot \sin\theta_{sun}}{\pi \cdot r_{ice} \cdot (r_{ice}^2 + h_{ice}^2)^{1/2}} \quad (14)$$

192 The ERA5 diffuse shortwave radiation is assumed to impact the conical Icestupa surface uniformly.

### 193 3.2.2 Net Longwave Radiation $q_{LW}$

194 The net longwave radiation  $q_{LW}$ , for which there were no direct measurements available at EP, is  
 195 determined as follows:

$$q_{LW} = LW_{in} - \sigma \cdot \epsilon_{ice} \cdot (T_{ice} + 273.15)^4 \quad (15)$$

196 where  $T_a$  represents the measured air temperature,  $T_{ice}$  is the modelled surface temperature, both  
 197 temperatures are given in  $^{\circ}\text{C}$ ,  $\sigma = 5.67 \cdot 10^{-8} \text{ J m}^{-2} \text{ s}^{-1} \text{ K}^{-4}$  is the Stefan-Boltzmann constant,  $LW_{in}$   
 198 denotes the incoming longwave radiation derived from the ERA5 dataset and  $\epsilon_{ice}$  is the corresponding  
 199 emissivity value for the Icestupa surface (see Table 1).

### 200 3.2.3 Turbulent sensible $q_S$ and latent $q_L$ heat fluxes

201 The turbulent sensible  $q_S$  and latent heat  $q_L$  fluxes are computed with the following expressions proposed  
 202 by Garratt (1992):

$$q_S = c_a \cdot \rho_a \cdot p_a / p_{0,a} \cdot \frac{\kappa^2 \cdot v_a \cdot (T_a - T_{ice})}{(\ln \frac{h_{AWS}}{z_{ice}})^2} \quad (16)$$

$$q_L = 0.623 \cdot L_s \cdot \rho_a / p_{0,a} \cdot \frac{\kappa^2 \cdot v_a (p_{v,a} - p_{v,ice})}{(\ln \frac{h_{AWS}}{z_{ice}})^2} \quad (17)$$

203 where  $h_{AWS}$  is the measurement height above the ground surface of the AWS (in  $m$ ),  $v_a$  is the wind  
 204 speed in  $\text{m s}^{-1}$  and  $M_F$  denotes fountain water spray mass in  $\text{kg}$ .  $c_a$  is the specific heat of air at  
 205 constant pressure ( $1010 \text{ J kg}^{-1} \text{ K}^{-1}$ ),  $\rho_a$  is the air density at standard sea level ( $1.29 \text{ kg m}^{-3}$ ),  $p_{0,a}$  is the air  
 206 pressure at standard sea level ( $1013 \text{ hPa}$ ),  $\kappa$  is the von Karman constant (0.4),  $L_s$  is the heat of sublimation  
 207 ( $2848 \text{ kJ kg}^{-1}$ ) and  $z_{ice}$  (1.7 mm) denotes the roughness length of ice (momentum and scalar). The vapor  
 208 pressures over air ( $p_{v,a}$ ) and ice ( $p_{v,ice}$ ) was obtained using the following formulation given in WMO  
 209 (2018):

$$\begin{aligned} p_{v,a} &= 6.107 \cdot 10^{(7.5 \cdot T_a / (T_a + 237.3))} \\ p_{v,ice} &= (1.0016 + 3.15 \cdot 10^{-6} \cdot p_a - 0.074 \cdot p_a^{-1}) \cdot (6.112 \cdot e^{(22.46 \cdot T_{ice} / (T_{ice} + 272.62))}) \end{aligned} \quad (18)$$

210 where  $p_a$  is the measured air pressure in  $\text{hPa}$ .

### 211 3.2.4 Fountain water heat flux $q_F$

212 The total energy flux is further influenced through the heat flux caused by the water that was additionally  
 213 added to the surface of the Icestupa during the time the fountain was running. We take this interaction  
 214 between the fountain water and the ice surface into account by assuming that the ice surface temperature  
 215 remains constant at  $0^{\circ}\text{C}$  during time steps when the fountain is active. This process can be divided into two  
 216 simultaneous steps: (a) the water temperature  $T_{water}$  is cooled to  $0^{\circ}\text{C}$  and (b) the ice surface temperature is  
 217 warmed to  $0^{\circ}\text{C}$ . Process (a) transfers the necessary energy for process (b) throughout the fountain runtime.  
 218 We further assume that this process is instantaneous, i.e. the ice temperature is immediately set to  $0^{\circ}\text{C}$   
 219 within just one time step  $\Delta t$  when the fountain is switched on. Thus, the heat flux caused by the fountain  
 220 water is calculated as follows:

$$q_F = \begin{cases} 0 & \text{if } \Delta M_F = 0 \\ \frac{\Delta M_F \cdot c_{water} \cdot T_{water}}{\Delta t \cdot A} + \frac{\rho_{ice} \cdot \Delta x \cdot c_{ice} \cdot T_{ice}}{\Delta t} & \text{if } \Delta M_F > 0 \end{cases} \quad (19)$$

221 with  $c_{ice}$  as the specific heat of ice.

### 222 3.2.5 Bulk Icestupa heat flux $q_G$

223 The bulk Icestupa heat flux  $q_G$  corresponds to the ground heat flux in normal soils and is caused by the  
224 temperature gradient between the surface layer ( $T_{ice}$ ) and the ice body ( $T_{bulk}$ ). It is expressed by using the  
225 heat conduction equation as follows:

$$q_G = k_{ice} \cdot (T_{bulk} - T_{ice}) / l_{ice} \quad (20)$$

226 where  $k_{ice}$  is the thermal conductivity of ice ( $2.123 \text{ W m}^{-1} \text{ K}^{-1}$ ),  $T_{bulk}$  is the mean temperature of the  
227 ice body within the Icestupa and  $l_{ice}$  is the average distance of any point in the surface to any other point in  
228 the ice body.  $T_{bulk}$  is initialised as  $0^\circ\text{C}$  and later determined from Eqn. 20 as follows:

$$T_{bulk}^{i+1} = T_{bulk} - (q_G \cdot A \cdot \Delta t) / (M_{ice} \cdot c_{ice}) \quad (21)$$

229 Since we assume a conical shape with  $r_{ice} > h_{ice}$ ,  $l_{ice}$  cannot be greater than  $2r_{ice}$  and also cannot  
230 be less than  $\Delta x$ . Therefore, the average distance from any point on the surface to any point inside is  
231  $\Delta x \leq l_{ice} \leq r_{ice}$ . We calculate  $q_G$  here assuming  $l_{ice} = r_{ice}/2$ .

### 232 3.2.6 Surface temperature changes and melt energy $q_{melt}$

233 The available net energy  $q_{net}$  partly increases surface temperature, but also contributes to ice melt at the  
234 surface of the Icestupa.  $q_T$  denotes the energy used on changing the surface temperature  $T_{ice}$  and  $q_{melt}$   
235 denotes the energy used to produce meltwater. So Eqn. 11 can be rewritten as:

$$q_{net} = q_{melt} + q_T \quad (22)$$

236 We define the freezing energy as  $q_{freeze} = (q_{net} - q_L)$ . This is because the latent heat always contributes  
237 to temperature fluctuations. Now, the temperature fluctuates based on three scenarios, namely (1) the  
238 freezing energy flux is negative but cannot freeze all the fountain water output; (2) the freezing energy flux  
239 is negative and can freeze all the fountain water output; (3) the freezing energy is positive or the fountain is  
240 inactive ( $\Delta M_F = 0$ ). Therefore, we express the rate of change of temperature as follows:

$$\frac{\Delta T}{\Delta t} = \begin{cases} -T_{ice}^{i-1} / \Delta t & \text{if } q_{freeze} < 0 \text{ and } \Delta M_F \geq -q_{freeze} \cdot A \cdot \Delta t / L_f \\ (\Delta M_F \cdot L_f) / (\rho_{ice} \cdot c_{ice} \cdot \Delta x \cdot A \cdot \Delta t) & \text{if } q_{freeze} < 0 \text{ and } \Delta M_F < -q_{freeze} \cdot A \cdot \Delta t / L_f \\ q_{net} / (\rho_{ice} \cdot c_{ice} \cdot \Delta x) & \text{if } \Delta M_F = 0 \text{ or } q_{freeze} > 0 \end{cases} \quad (23)$$

241 Whenever the model predicts  $T_{ice}^{i+1} > 0^\circ\text{C}$ , then the surface temperature is set to  $0^\circ\text{C}$  in the corresponding  
242 time step and additional energy contributes to  $q_{melt}$ . Combining these requirements, we get:

$$(q_T, q_{melt}) = \begin{cases} (\rho_{ice} \cdot c_{ice} \cdot \Delta x \cdot \frac{\Delta T}{\Delta t}, q_{net} - q_L - \rho_{ice} \cdot c_{ice} \cdot \Delta x \cdot \frac{\Delta T}{\Delta t}) & \text{if } T_{ice}^{i+1} \leq 0^\circ\text{C} \text{ and } \Delta M_F > 0 \\ (\rho_{ice} \cdot c_{ice} \cdot \Delta x \cdot \frac{\Delta T}{\Delta t}, q_{net} - \rho_{ice} \cdot c_{ice} \cdot \Delta x \cdot \frac{\Delta T}{\Delta t}) & \text{if } T_{ice}^{i+1} \leq 0^\circ\text{C} \text{ and } \Delta M_F = 0 \\ (-\rho_{ice} \cdot c_{ice} \cdot \Delta x \cdot \frac{T_{ice}^i}{\Delta t}, q_{net} - q_L + \rho_{ice} \cdot c_{ice} \cdot \Delta x \cdot \frac{T_{ice}^i}{\Delta t}) & \text{if } T_{ice}^{i+1} > 0^\circ\text{C} \text{ and } \Delta M_F > 0 \\ (-\rho_{ice} \cdot c_{ice} \cdot \Delta x \cdot \frac{T_{ice}^i}{\Delta t}, q_{net} + \rho_{ice} \cdot c_{ice} \cdot \Delta x \cdot \frac{T_{ice}^i}{\Delta t}) & \text{if } T_{ice}^{i+1} > 0^\circ\text{C} \text{ and } \Delta M_F = 0 \end{cases} \quad (24)$$

**Table 1.** Free parameters in the model categorised as constant, uncertain and site parameters. Base value (B) and uncertainty (U) were taken from the literature. For assumptions (assum.), the uncertainty was chosen to be relatively large (5 %). For measurements (meas.), the uncertainty due to parallax errors is chosen to be (1 %).

Constant Parameters	Symbol	Value	References
Van Karman constant	$\kappa$	0.4	B: Cuffey and Paterson
Stefan Boltzmann constant	$\sigma$	$5.67 \cdot 10^{-8} W m^{-2} K^{-4}$	B: Cuffey and Paterson
Air pressure at sea level	$p_{0,a}$	1013 hPa	B: Mölg and Hardy
Density of water	$\rho_w$	$1000 kg m^{-3}$	B: Cuffey and Paterson
Density of ice	$\rho_{ice}$	$917 kg m^{-3}$	B: Cuffey and Paterson
Density of air	$\rho_a$	$1.29 kg m^{-3}$	B: Mölg and Hardy
Specific heat of water	$c_w$	$4186 J kg^{-1} ^\circ C^{-1}$	B: Cuffey and Paterson
Specific heat of ice	$c_{ice}$	$2097 J kg^{-1} ^\circ C^{-1}$	B: Cuffey and Paterson
Specific heat of air	$c_a$	$1010 J kg^{-1} ^\circ C^{-1}$	B: Mölg and Hardy
Thermal conductivity of ice	$k_{ice}$	$2.123 W m^{-1} K^{-1}$	B: Bonales et al.
Latent Heat of Sublimation	$L_s$	$2848 kJ kg^{-1}$	B: Cuffey and Paterson
Latent Heat of Evaporation	$L_e$	$2514 kJ kg^{-1}$	B: Cuffey and Paterson
Latent Heat of Fusion	$L_f$	$334 kJ kg^{-1}$	B: Cuffey and Paterson
Gravitational acceleration	$g$	$9.81 m s^{-2}$	B: Cuffey and Paterson
Uncertain Parameters		Range	
Precipitation	$T_{ppt}$	$1 ^\circ C$	$\pm 1 ^\circ C$
Temperature threshold			B + U: Fujita and Ageta, Zhou et al.
Ice Emissivity	$\epsilon_{ice}$	0.95	[0.949,0.993] B: Cuffey and Paterson; U: Hori et al.
Ice Albedo	$\alpha_{ice}$	0.35	$\pm 5 \%$ B: Cuffey and Paterson; U: assum.
Snow Albedo	$\alpha_{snow}$	0.85	$\pm 5 \%$ B: Cuffey and Paterson; U: assum.
Albedo Decay Rate	$\tau$	10 days	[1, 22] days B: Schmidt et al.; U: Oerlemans and Knap assum.
Ice layer thickness	$\Delta x$	5 mm	[1, 10] mm
Site Parameters			
Fountain diameter	nozzle	$dia_F$	5 mm $\pm 1 \%$ B: meas. ; U: assum.
Fountain height		$h_F$	$\pm 1 \%$ B: meas. ; U: assum.
Fountain temperature	water	$T_{water}$	$[0, 9] ^\circ C$ B: meas. ; U: meas.
AWS height		$h_{AWS}$	$\pm 1 \%$ B: meas. ; U: assum.

243 **3.3 Mass Balance**

244 The mass balance equation is used to derive the water that drains away ( $M_{runoff}$ ) as follows:

$$\frac{\Delta M_{runoff}}{\Delta t} = \frac{\Delta M_F + \Delta M_{ppt} + \Delta M_{dpt} + \Delta M_{cdt} - \Delta M_{ice} - \Delta M_{melt} - \Delta M_{vapour}}{\Delta t} \quad (25)$$

245 where  $\Delta M = M^i - M^{i-1}$ . Here  $\frac{\Delta M_F}{\Delta t} = d_F$  where  $d_F$  is the spray of the fountain measured in  $[kg s^{-1}]$ ;  
 246  $M_{ppt}$  is the cumulative precipitation;  $M_{dpt}$  is the cumulative accumulation through water vapour deposition;  
 247  $M_{cdt}$  is the cumulative accumulation through water vapour condensation;  $M_{ice}$  is the cumulative mass of  
 248 ice;  $M_{melt}$  is the cumulative mass of melt water and  $M_{vapour}$  represents the cumulative water vapor loss  
 249 by evaporation or sublimation.

250 Precipitation input is calculated as:

$$\frac{\Delta M_{ppt}}{\Delta t} = \begin{cases} \pi \cdot r_{ice}^2 \cdot \rho_w \cdot ppt & \text{if } T_a < T_{ppt} \\ 0 & \text{if } T_a \geq T_{ppt} \end{cases} \quad (26)$$

251 where  $\rho_w$  is the density of water ( $1000 kg m^{-3}$ ),  $ppt$  is the measured precipitation rate in  $[m s^{-1}]$  and  
 252  $T_{ppt}$  is the temperature threshold below which precipitation falls as snow. Here, snowfall events were  
 253 identified using  $T_{ppt}$  as  $1^\circ C$ . Snow mass input is calculated by assuming a uniform deposition over the  
 254 entire circular footprint of the Icestupa.

255 The latent heat flux is used to estimate either the evaporation and condensation processes or sublimation  
 256 and deposition processes. To differentiate between these two possibilities, we classify the time steps into  
 257 humid or non-humid depending on whether the corresponding relative humidity value is above or below  
 258 60% (Stigter et al., 2018). On humid time steps, we assume condensation or evaporation to occur whereas  
 259 on non-humid time steps deposition or sublimation can occur. Correspondingly, latent heat of evaporation  
 260 ( $L_e$ ) is used for humid time steps and latent heat of sublimation ( $L_s$ ) is used for non-humid time steps.

$$\left( \frac{\Delta M_{vapour}}{\Delta t}, \frac{\Delta M}{\Delta t} \right) = \begin{cases} (-q_L \cdot A/L, 0) & \text{if } q_L < 0 \\ (0, q_L \cdot A/L) & \text{if } q_L \geq 0 \end{cases} \quad (27)$$

261 where  $L = \begin{cases} L_s & \text{if } RH < 60 \\ L_e & \text{if } RH \geq 60 \end{cases}$  and  $M = \begin{cases} M_{dpt} & \text{if } RH < 60 \\ M_{cdt} & \text{if } RH \geq 60 \end{cases}$

262 Deposition or sublimation process involves phase change between ice and vapour. Condensation or  
 263 evaporation process involves phase change between water and vapour. To account for this difference, we  
 264 define the following terms:

$$(\Delta M_{ice}^*, \Delta M_{melt}^*) = \begin{cases} (\Delta M_{ice} + \Delta M_{vapour} - \Delta M_{dpt}, \Delta M_{melt}) & \text{if } RH < 60 \\ (\Delta M_{ice}, \Delta M_{melt} + \Delta M_{vapour} - \Delta M_{cdt}) & \text{if } RH \geq 60 \end{cases} \quad (28)$$

265 Using the melt energy  $q_{melt}$ , we estimate the frozen and melted ice mass ( $\Delta M_{ice}$ ,  $\Delta M_{melt}$ ). Removing  
 266 the contribution of precipitation and combining Eqn. 27 and Eqn. 28 we are left with the contribution from  
 267 the melt energy as follows:

**Table 2.** Summary of mass balance components for the EP experiment after the fountain spray was stopped (on 15<sup>th</sup> February 2019) and at the end of the model run (on 5<sup>th</sup> April). All parameters except  $M_F$  were modelled.

	Mass Component	Fountain spray ends	Model ends
Input	$M_F$	18060 kg	18060 kg
	$M_{ppt}$	444 kg	466 kg
	$M_{dpt}$ $M_{cdt}$	0 kg 7 kg	0 kg 32 kg
Output	$M_{melt}$	163 kg	1013 kg
	$M_{ice}$	809 kg	0 kg
	$M_{vapour}$ $M_{runoff}$	11 kg 17529 kg	16 kg 17529 kg

$$\left( \frac{\Delta M_{ice}^* - \Delta M_{ppt}}{\Delta t}, \frac{\Delta M_{melt}^*}{\Delta t} \right) = \begin{cases} \frac{q_{melt} \cdot A}{L_f} \cdot (-1, 1) & \text{if } q_{melt} \geq 0 \\ \frac{q_{melt} \cdot A}{L_f} \cdot (-1, 0) & \text{if } q_{melt} < 0 \text{ and } \frac{\Delta M_F}{\Delta t} \geq -\frac{q_{melt} \cdot A}{L_f} \\ \left( \frac{\Delta M_F}{\Delta t}, 0 \right) & \text{if } q_{melt} < 0 \text{ and } 0 \leq \frac{\Delta M_F}{\Delta t} < -\frac{q_{melt} \cdot A}{L_f} \end{cases} \quad (29)$$

268 Now, with all the other terms known in Eqn. 25, the water drainage/runoff can be determined.

269 Considering AIRs as water reservoirs, we can quantify their potential through the amount of water they  
270 store (storage quantity) and the length of time they store it (storage duration). Another means of comparing  
271 different Icestupas is through their water storage efficiency defined accordingly as:

$$\text{Storage Efficiency} = \frac{M_{melt}}{(M_F + M_{ppt} + M_{dpt} + M_{cdt})} \cdot 100 \quad (30)$$

## 4 MODEL RESULTS

272 The model was forced with meteorological data from 30<sup>th</sup> January to 5<sup>th</sup> April 2019 (Fig. 3) and various  
273 parameters (see Table 1) to calculate the mass and energy balance of the Icestupa.

### 4.1 Energy and mass balance calculation

275 Daily averages of some components of the energy balance are shown in Fig. 6 (b). On average during  
276 the experiment duration, the total energy balance was almost zero. Net shortwave radiation ( $33 \text{ W m}^{-2}$ ),  
277 sensible ( $10 \text{ W m}^{-2}$ ) and latent heat flux ( $2 \text{ W m}^{-2}$ ) with a mostly positive flux towards the surface of the  
278 icestupa were compensated by the net longwave radiation ( $-34 \text{ W m}^{-2}$ ) and the melt energy ( $-12 \text{ W m}^{-2}$ ).  
279 The contributions of other fluxes were negligible in comparison.

280 Net shortwave radiation is the main input to, and the most varying energy flux on the ice surface. Its  
281 variability is controlled by the surface albedo  $\alpha$  and the area fraction  $f_{cone}$  which therefore represent key  
282 variables in the energy balance (Fig. 7 (b)). Although global radiation flux reached a daily maximum  
283 value of  $339 \text{ W m}^{-2}$ ,  $q_{sw}$  only went up to  $98 \text{ W m}^{-2}$ . This is caused by the fact that only about 30 % of  
284 the direct solar radiation influenced the Icestupa surface as shown by the area fraction  $f_{cone}$  in Fig. 7 (a).

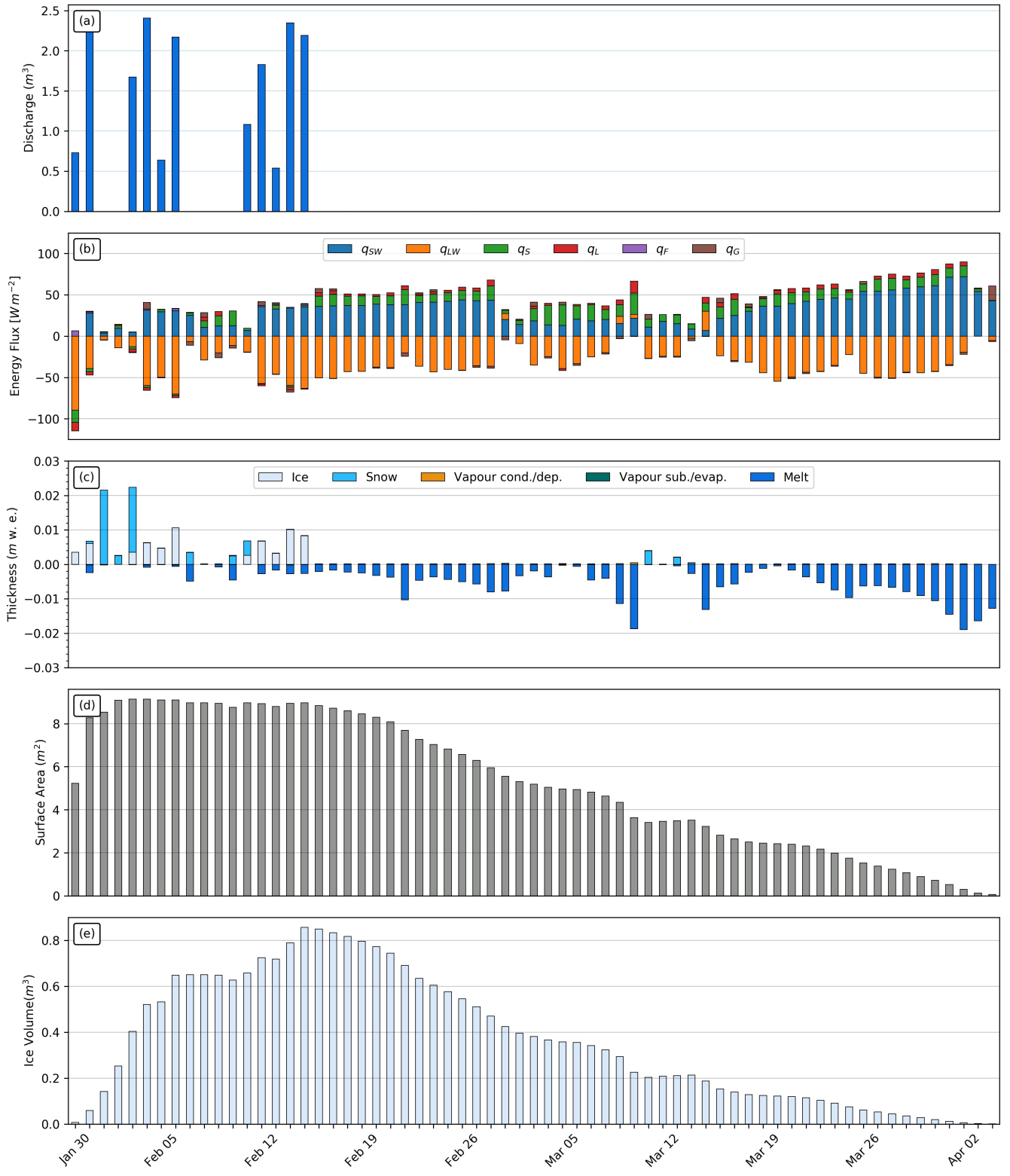


**Figure 6.** (a) Fountain discharge (b) energy flux components, (c) mass flux components (d) surface area and (e) volume of the Icestupa in daily time steps.  $q_{SW}$  is the net shortwave radiation;  $q_{LW}$  is the net longwave radiation;  $q_L$  and  $q_S$  are the turbulent latent and sensible heat fluxes.  $q_F$  represents the interactions of the ice-water boundary during fountain on time steps.  $q_G$  quantifies the heat conduction process between the Icestupa surface layer and the ice body.

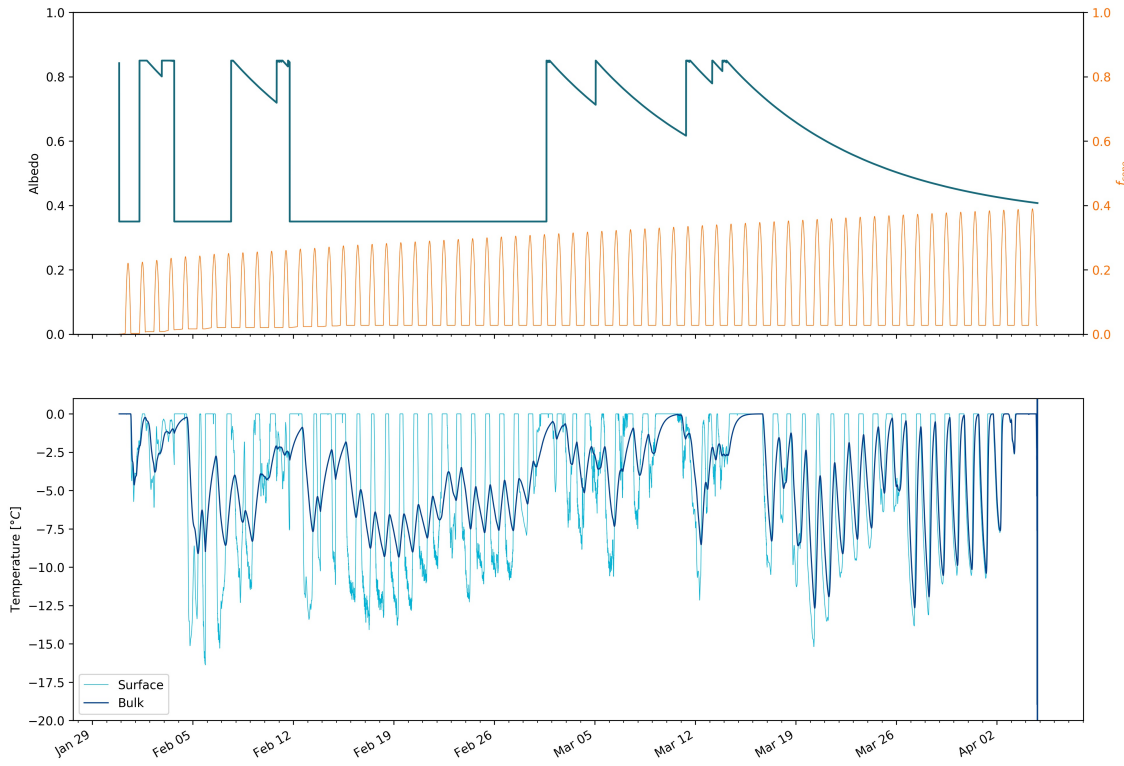


**Figure 7.** Some derived parameters of the model, namely, albedo and  $f_{cone}$  (a), Surface and bulk temperature (b). In (a), the green curve shows how snow and fountain-on events reset albedo between ice albedo and snow albedo. The decay of the snow albedo to ice albedo can also be observed. The orange curve shows how the solar radiation area fraction varied diurnally with variations in the solar elevation angle. In (b), the surface temperature (light blue curve) was forced to be 0 °C during fountain activity. The corresponding bulk temperature is shown with the dark blue curve.

285 Snowfall is the atmospheric variable connected most closely and proportionally to albedo. Higher and/or  
 286 more frequent snowfall thus decreases the energy available for melt due to the corresponding increase in  $\alpha$ .  
 287  $q_{LW}$  was predominantly negative indicating that this energy balance component drove the freezing of  
 288 the ice structure. Daily values of  $q_{LW}$  ranged from -89 to 21  $Wm^{-2}$ . Turbulent sensible heat flux  $q_S$   
 289 contributed mostly to the melt of the ice structure. Daily values of  $q_S$  ranged from -14 to 26  $Wm^{-2}$ .  
 290 Deposition/condensation was favored over evaporation/sublimation during 95 % of the model runtime.  
 291 Daily values of the turbulent latent heat flux  $q_L$  ranged from -10 to 15  $Wm^{-2}$ . Since the mean of  $q_L$  was  
 292 positive, the Icestupa gained mass cumulatively from the atmosphere due to the condensation process.  
 293 Fountain water heat flux  $q_F$  had a mean of zero as it was only nonzero during 1002 time steps or around  
 294 100 hours. Daily values of  $q_F$  ranged from -1 to 6  $Wm^{-2}$ . The contribution of heat flux by conduction  
 295  $q_G$  was also minimal as it only varied between -6 to 12  $Wm^{-2}$  with a mean of 0  $Wm^{-2}$ . The energy  
 296 contributing to surface temperature changes ( $q_T$ ) was insignificant in comparison to the energy spent on  
 297 freezing and melting ( $q_{melt}$ ). The resulting bulk temperature and the surface temperature are shown in Fig.  
 298 7 (b). For the total considered period,  $q_{LW}$  accounted for 33.8% of overall energy turnover. The energy  
 299 turnover is calculated as the sum of energy fluxes in absolute values.  $q_{SW}$  accounted for 31.3%, followed  
 300 by  $q_{melt}$  (19%),  $q_S$  (9.6%),  $q_L$  (3.6%),  $q_G$  (2.4%),  $q_F$  (0.2%) and  $q_T$  (0.4%).

301 Fig. 6 (c) represents the mass fluxes associated with these energy exchanges expressed in m w.e. It  
 302 shows the ice and meltwater formed due to  $q_{melt}$ , snow accumulated due to precipitation, water vapour

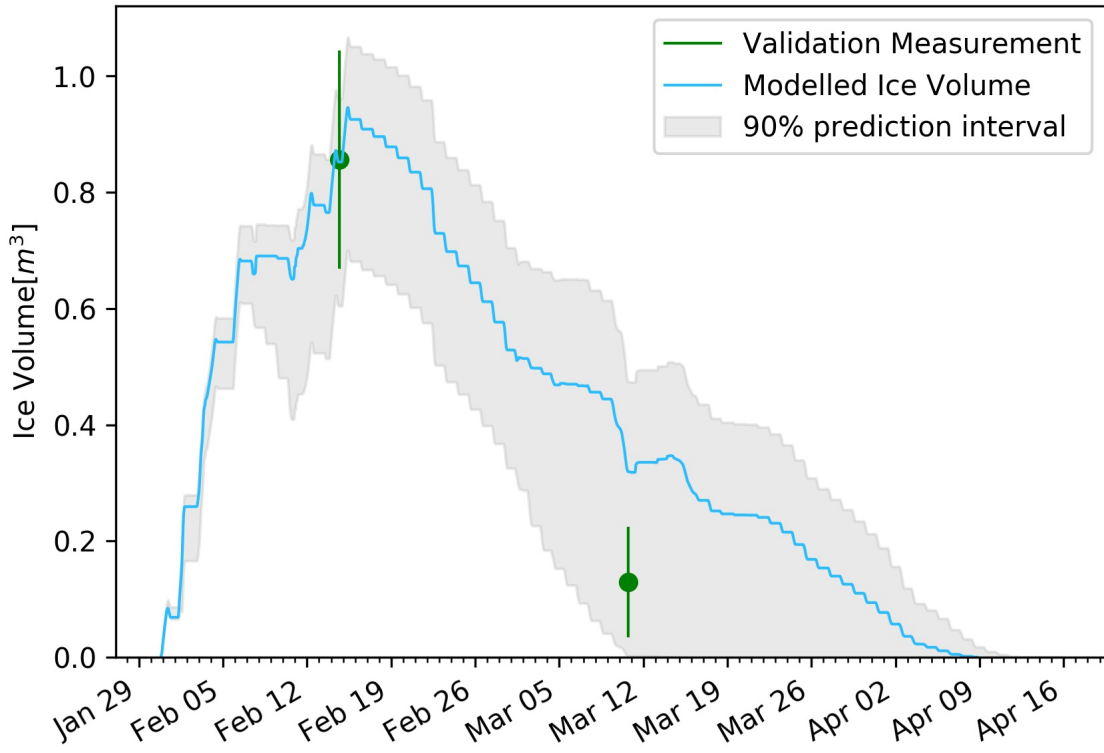


**Figure 8.** Modelled ice volume during the lifetime of the EP Icestupa (blue curve). Green line segments indicate the first and second validation measurements. The prediction interval is based on the ice volume uncertainty caused by the most sensitive parameters, namely, temperature threshold below which precipitation falls as snow and the ice emissivity.

303 deposition/condensation and sublimation/evaporation due to  $q_L$ . Growth rate ( $\frac{\Delta M_{ice}}{\Delta t}$ ) shows a strong  
 304 correlation with net energy flux ( $r^2 = 0.31$ ) but poor correlation with Icestupa surface area ( $r^2 = 0.03$ ).  
 305 This is because the variance in growth rate is mostly due to the variance in  $q_{net}$  as illustrated in Fig. 6.  
 306 Since  $r_{ice}$  was initialised with the spray radius  $r_F$ , the surface area maintains a maximum initially until the  
 307 energy flux becomes positive. This trend favours the positive over the negative thickness changes resulting  
 308 in a steep increase and gradual melting of ice volume as can be seen in Fig. 8.

309 The total water used for the Icestupa development includes contributions from the fountain (97.3%),  
 310 snowfall (2.5 %), condensation (0.2 %) as shown in Table 2. The maximum ice mass during the whole  
 311 measurement period was 809 kg, which occurred after the last fountain run on Feb 16<sup>th</sup> 2019 in the morning.  
 312 Therefore, in the case of EP we used a water input of 18,558 kg, with a resultant storage efficiency of only  
 313 5.5 %.

## 5 MODEL SENSITIVITY AND UNCERTAINTY ANALYSIS

314 The icestupa model can be regarded as a function  $f(x_1, x_2 \dots, x_n) = (y_1, y_2 \dots, y_m)$ , where  
 315  $(x_1, x_2 \dots, x_n)$  are the model parameters and  $(y_1, y_2 \dots, y_m)$  are the model outputs. The influence of each  
 316 parameter on the output variables of interest were quantified and the most important physical parameters  
 317 for the subsequent uncertainty analysis were determined. The sensitivity of a parameter  $x_j$  is determined  
 318 by keeping all other parameters  $x_i, i \neq j$  fixed at their baseline value and varying  $x_j$  within values that are  
 319 physically plausible.

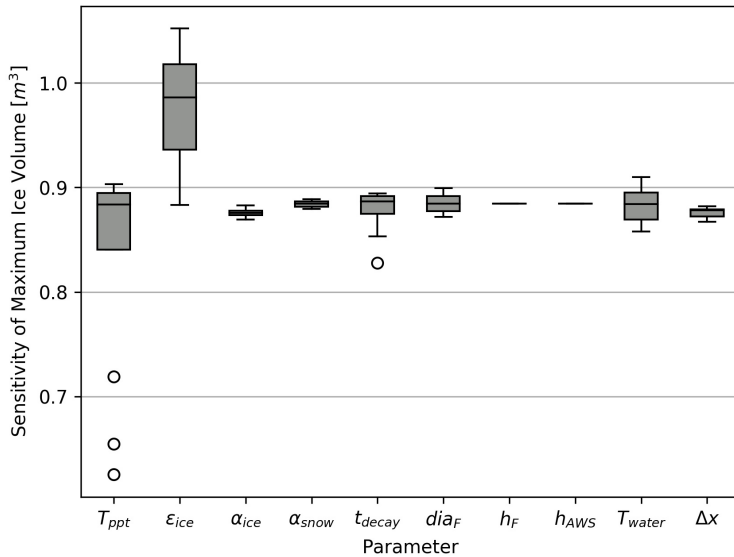


**Figure 9.** Sensitivities of maximum ice volume to all the uncertain and site parameters used in the model (Table 1). Outliers in the bar plot are shown as 'o'.

320 A sensitivity study on the parameters (listed in Table 1) was performed with the maximum ice volume  
 321 as the target variable. All the parameters were assumed to be independent of each other with a uniform  
 322 distribution. This assumption ignores the auto-correlation present among the parameters associated with  
 323 the albedo parameterisation. The range of uncertain parameters were set based on available literature values  
 324 or varied  $\pm 5\%$  from the base value if no such reference was available. The uncertainty of all the site  
 325 parameters were caused due to parallax errors during manual measurement. This was quantified with a  
 326 range of  $\pm 1\%$  from the base value. However, it must be kept in mind that, even though intended to be as  
 327 objective as possible, the selection of a parameter range has a subjective part that influences the results and  
 328 conclusions obtained in this analysis. The variation of the model outputs  $y_k$  is evaluated to quantify the  
 329 local sensitivities  $s_{j,k}$  that are defined here as the 95% range of the simulated outputs.

330 To perform the uncertainty analysis, we included only parameters that influence the maximum ice volume  
 331 by at least  $0.1 m^3$ . All other parameters were fixed at their baseline value. Fig. 9 shows all the variance  
 332 produced by these uncertain parameters in maximum ice volume calculation. It shows that  $\epsilon_{ice}$  and  $T_{ppt}$  are  
 333 the only parameters with a maximal sensitivity of more than  $0.1 m^3$  for the maximum ice volume estimate.  
 334 Consequently, all other parameters were excluded from the subsequent uncertainty analysis.

335 The temperature threshold below which precipitation falls as snow ( $T_{ppt}$ ) was found to be the most  
 336 sensitive parameter. It is used in the model to reset the albedo to snow albedo and determine snow  
 337 precipitation events. The lower  $T_{ppt}$  parameter the higher the albedo (as the Icestupa surface has a lower  
 338 albedo when ice-covered than when snow-covered). The variation of  $T_{ppt}$  by  $\pm 1^\circ C$  caused maximum ice  
 339 volume variation of  $0.84 \pm 0.2 m^3$ .

340 Ice emissivity was also found to be a sensitive parameter. The higher the ice emissivity the larger the  
 341 maximum ice volume as the emitted longwave radiation increases with ice emissivity. Variation of  $\epsilon_{ice}$  by  
 342 5% caused a maximum ice volume range from  $0.98 \pm 0.1 m^3$ .

343 In total, the sensitivity analysis required 120 simulations, and the uncertainty analysis a total of 32  
 344 simulations.

## 6 DISCUSSION

### 345 6.1 Model validation quality

346 We first evaluate the model against the validation measurements at the EP site. The uncalibrated model  
 347 is able to capture both the freezing and the melting process sufficiently well as the modelled ice volume  
 348 lies within the uncertainty of both validation measurements. Furthermore, the validation measurements fit  
 349 well within the estimated model uncertainty. However, since this validation is based on only two points, it  
 350 does limit the confidence in the model results. Even though the model estimates validate well with the ice  
 351 volume, the same is not the case for the surface area. The surface area estimated from the first validation  
 352 measurement is just around  $4 m^2$ , roughly half the model estimated surface area. However, the validation  
 353 surface area estimate again underestimates the surface area as the actual surface area in contact with the  
 354 atmosphere could have been amplified by the inherent roughness of the ice surface. Another major cause of  
 355 this discrepancy was the conical shape assumption, as in reality, the Icestupa shape ranged between a cone  
 356 and a cylinder (Fig. 2). The sensitivity of the model results to these errors was further amplified due to the  
 357 relatively small volume of the EP Icestupa. In summary, better and frequent validation measurements on a  
 358 more voluminous Icestupa would have increased confidence on the model results.

### 359 6.2 Important assumptions

360 In the sensitivity and uncertainty analysis presented above, we did not account for several general  
 361 assumptions and parametrisation choices that may cause model errors. Some assumptions and their  
 362 potential to cause errors are discussed below.

- 363 • Turbulent Sensible and Latent Heat Fluxes: The method used to calculate the turbulent heat fluxes  
 364 by Garratt (1992) assumes that the turbulent heat fluxes are acting over a uniform planar surface to  
 365 determine the roughness length. Since our application is on a conical surface, the distance to the ice  
 366 surface is not uniform and well defined. Hence,  $z_{ice}$  has no real physical significance here.
- 367 • Droplet flight time loss: Water losses during the flight time of fountain droplets were neglected making  
 368 all the fountain spray available for freezing. For the EP experiment, inclusion of this parameter does  
 369 not influence results since it is already accounted for in the runoff water discharge rate which was at  
 370 least  $3 l min^{-1}$ .
- 371 • Nucleation of droplets: Corresponding to droplet flight time, ice/snow formation is also possible before  
 372 surface contact if nucleation occurs during flight time. For the EP experiment, this process will further  
 373 increase the freeze rate and hence the storage efficiency. This process is neglected for model simplicity.
- 374 • Shape Effects: The suppression of heat exchange between the snow/ice surface and the air adjacent  
 375 to the surface effectively slows down snow/ice ablation in spring and promotes the stagnation of the  
 376 cold air within topographical depressions (Fujita et al., 2010). The quantitative contribution of the  
 377 atmospheric decoupling over melting snow/ice for the total mass and energy balance is ignored in the  
 378 model.

### 379 6.3 Icestupa construction decisions

380 There are several decisions one has to take when constructing Icestupas. These can be broadly divided  
 381 into two types of decisions, namely location and fountain decisions. Both the meteorological conditions  
 382 of the location and the surface area produced by the fountain significantly influence the observed growth  
 383 rate. Since our validation is restricted to just one location, we restrict our discussion to the optimization  
 384 possibilities of Icestupa constructions through fountain decisions.

385 Assuming a constant spray for the fountain, we can divide the fountain decisions into fountain state  
 386 (on/off) and type (height and nozzle diameter). From an energy balance point of view, the fountain should

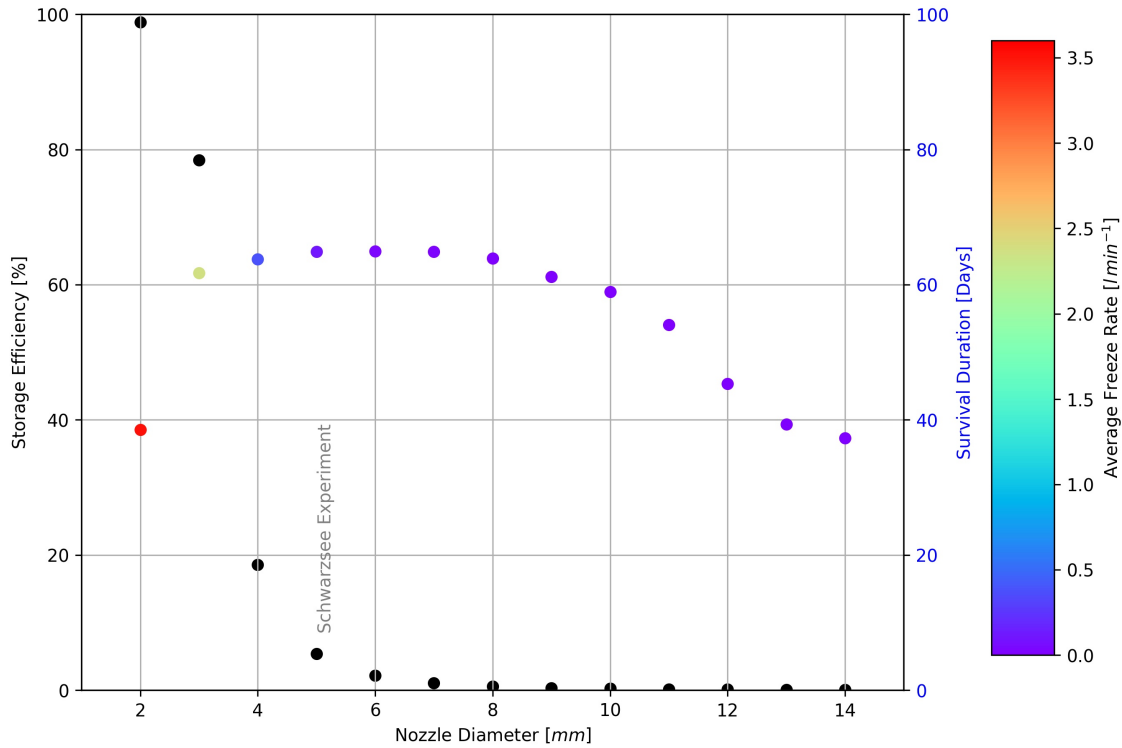


**Figure 10.** Variation in storage efficiency (black dots) and storage duration (coloured dots) with changes in fountain's nozzle diameter. The dot colours represent average freeze rate based on the color bar.

387 be switched on for all time intervals when  $q_{net} < 0$  which would have increased the fountain discharge  
 388 duration from 90 hours to 850 hours. However, in our experiment, the fountain state decision was set on the  
 389 basis of prior Icestupa construction experience where a critical temperature of  $-5^{\circ}\text{C}$  was recommended.  
 390 But ambient temperature was a poor indicator of  $q_{net}$  ( $r^2 = 0.17$ ). Therefore, using air temperature to  
 391 determine when the fountain should be switched on was not ideal.

392 The fountain type used can be characterised by the physical structure of the fountain, namely its height and  
 393 nozzle diameter. Maintaining the same spray rate and height, one can optimize the Icestupa development  
 394 by identifying the minimum nozzle diameter that yields the maximum storage efficiency. Since we never  
 395 changed the fountain height for the EP Icestupa, we only focus on optimization of fountain diameter below.

396 Fig. 10 shows reducing the nozzle diameter to 3 mm increases storage efficiency up to 78 % without  
 397 compromising much on storage duration. The corresponding storage quantity of the 3 mm nozzle diameter  
 398 was more than 23 times higher than the 5 mm fountain used in our experiment. This is because the spray  
 399 radius  $r_F$  of the 3 mm fountain was much higher at 8.5 m compared to the 1.7 m spray radius of the 5  
 400 mm fountain. Here, we define growth rate as freeze rate when fountain is active and melt rate otherwise.  
 401 Therefore, this higher spray radius both increases the freeze rate and increases the melt rate since they are  
 402 both directly proportional to the surface area. However, since the freeze rate cannot increase beyond a spray  
 403 rate of  $3.6 \text{ lmin}^{-1}$  (except during precipitation or deposition/condensation events), an optimum spray  
 404 radius or nozzle diameter exists, beyond which storage duration suffers due to a disproportionate increase  
 405 in melt rate compared to the freeze rate. So even though 3 mm nozzle diameter had a much higher storage  
 406 quantity than the 5 mm nozzle, its storage duration was around 2 days less than the 5 mm nozzle. One  
 407 physical cause of this effect is the different shapes of both the ice structures. A flat sheet of ice (effectively

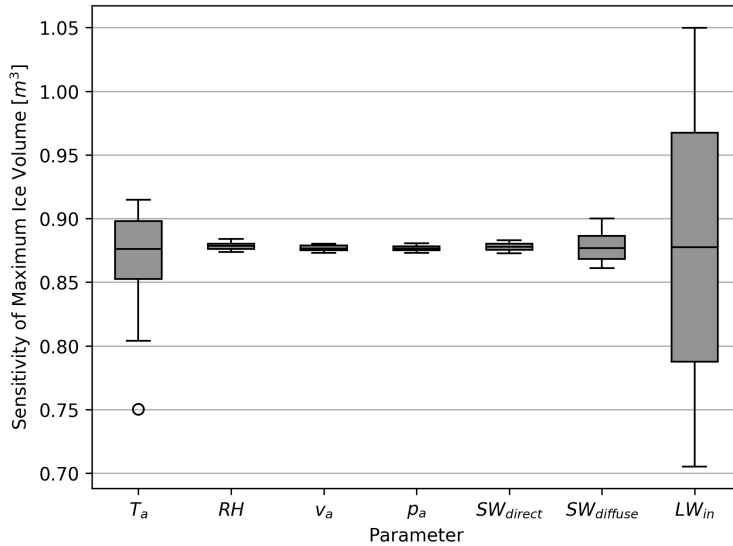


**Figure 11.** Sensitivities of maximum ice volume to all the meteorological input parameters used in the model (Figure 3). Outliers in the bar plot are shown as 'o'.

408 a cone with a high spray radius) with higher mass might have a storage duration shorter than a conical ice  
 409 structure. As the spray radius decreases with increasing nozzle diameter, the ice structure's average slope  
 410 increases and so the 5 mm nozzle's ice structure is "more" conical than the 3 mm ice structure. Fig. 10  
 411 shows that a nozzle diameter of 3 mm has an average freeze rate ( $2.4 \text{ l min}^{-1} \text{ w.e.}$ ) which is large enough  
 412 to increase the storage efficiency and small enough to not reduce the storage duration of the Icestupa  
 413 significantly.

#### 414 6.4 Meteorological sensitivity

415 The sensitivity of maximum ice volume associated with changes in meteorological parameters was  
 416 quantified. The meteorological parameters include  $T_a$ ,  $RH$ ,  $v_a$ ,  $p_a$ ,  $SW_{direct}$ ,  $SW_{diffuse}$  and  $LW_{in}$ . In  
 417 each perturbation scenario, a certain meteorological parameter was perturbed to a certain extent. Among  
 418 those changes,  $T_a$  was absolute changes ( $\pm 1^\circ\text{C}$ ) and other parameters were relative variations ( $\pm 5\%$ ).  
 419 All perturbations were implemented uniformly in space on the modeling domain and in time through the  
 420 modeling periods. To separate the effects of individual meteorological parameters, only one parameter was  
 421 changed in each case, while all the other parameters were kept unchanged. Please note that these types of  
 422 perturbations are not what happens in the real world, where meteorological parameters are inter-linked.

423 As can be seen from Fig. 11, the maximum ice volume is most sensitive to  $LW_{in}$ . This suggests that  
 424 there could be significant influence of nearby topological features on the growth rate of the Icestupa even  
 425 within the same valley. Hence choice of appropriate location with minimal exposure to longwave radiation  
 426 is crucial.

#### 427 6.5 Schwarzsee vs Leh Icestupa

428 It could be argued that the relatively small EP Icestupa cannot be compared with the much larger Icestupas  
 429 in Ladakh which store millions of litres of water for several months (see Appendix 8.1). However, this is  
 430 the only Icestupa dataset currently available for such a model validation.

431 Table 2 clearly shows that for our EP experiment most of the input water (94.5 %) simply drained away  
 432 ( $M_{runoff}$ ). This high water loss through drainage is due to the fact that the average spray rate of the fountain

433  $((\frac{\Delta M_F}{\Delta t})_{mean} = 3.6 \text{ l min}^{-1})$  far exceeded the max Icestupa growth rate ( $((\frac{\Delta M_{ice}}{\Delta t})_{max} = 0.9 \text{ l min}^{-1}$  (w.e.)  
 434 ).

435 In the city of Leh, Ladakh at an altitude of 3500 m a.s.l. the air temperature shows values down to  
 436  $-27.9^\circ\text{C}$  in winter (Chevuturi et al., 2018) whereas EP had a minimum temperature of just  $-11.6^\circ\text{C}$   
 437 during the study period. Moreover, subzero temperatures were only reached for 7 nights of fountain  
 438 operation at the EP site compared to the 43 nights of fountain operation possible in Ladakh (see Appendix  
 439 8.1). Thus, the Icestupa growth rate is expected to be much higher in Ladakh. However, water spray rates  
 440 in Ladakh are also much higher (around  $210 \text{ l min}^{-1}$ ). This suggests that the water losses in Ladakh could  
 441 be caused by excessive fountain spray.

## 7 CONCLUSIONS

442 We outlined a methodology for estimating ice, liquid water, water vapour and runoff quantities produced  
 443 during the construction of an Icestupa using measurements of fountain spray rate, air temperature, radiation,  
 444 humidity, pressure, wind and cloudiness at the EP study site. The comparison with validation measurements  
 445 at two different dates during the experiment led to satisfying results, although a more rigorous model  
 446 validation was not possible due to few icestupa volume measurements.

447 According to the model, the EP Icestupa achieved a storage quantity of 1005 litres of water with a storage  
 448 duration of 65 days. However, the corresponding storage efficiency of 6 % was very low for a water input of  
 449 18,560 litres. These estimates were most sensitive to the temperature threshold that determined precipitation  
 450 phase and ice emissivity parameters which created an uncertainty of  $0.2\text{m}^3$  in the maximum ice volume  
 451 calculated. This is to be expected as net longwave radiation and net shortwave radiation together accounted  
 452 for around 65 % of the overall energy turnover.

453 Although the location, storage quantity and duration of our experimental EP Icestupa are not representative  
 454 of the much larger Icestupas of Ladakh, the model results do support the hypothesis that there could be  
 455 considerable water loss during the formation of Icestupas particularly due to excessive fountain spray.  
 456 Using model calculations, it was shown that a decreased fountain nozzle diameter of 3 mm can increase the  
 457 storage efficiency drastically. This is because a change in the fountain nozzle diameter causes an effective  
 458 change of the ice surface area over which the net energy flux can act. This result has relevance on the future  
 459 design of Icestupa fountains. However, care has to be taken as our model is currently only validated by one  
 460 experiment at the EP site. Further experiments at different locations with different fountains are required to  
 461 better understand the influence of construction decisions on the results.

## 8 APPENDIX

### 462 8.1 Ladakh Icestupa 2014/15

463 A 20 m tall Icestupa (Wangchuk, 2015c) was built in Phyang village, Ladakh at an altitude of 3500  
 464 m a.s.l. Assuming a conical shape with a diameter of 20 m, the corresponding volume of this Icestupa  
 465 becomes  $2093 \text{ m}^3$  or  $1,920 \text{ m}^3$  w.e. The fountain sprayed water at a rate of  $210 \text{ l min}^{-1}$  (Wangchuk,  
 466 2015e) from 21<sup>st</sup> January (Wangchuk, 2015a) to at least until 5<sup>th</sup> March 2015 (Wangchuk, 2015b) (around  
 467 43 nights). Assuming fountain spray was active for 8 hours each night, we estimate water consumption to  
 468 be around  $4,334 \text{ m}^3$ . Thus, during the construction/freezing period of the Icestupa, roughly 56 % of the  
 469 water provided was wasted. The actual water loss is bound to be much higher due to further vapour losses  
 470 during the melting period. This Icestupa completely melted away on 6<sup>th</sup> July 2015 (Wangchuk, 2015d).  
 471 Therefore, the storage duration was 166 days or roughly 5 months.

## CONFLICT OF INTEREST STATEMENT

472 The authors declare that the research was conducted in the absence of any commercial or financial  
473 relationships that could be construed as a potential conflict of interest.

## AUTHOR CONTRIBUTIONS

474 SB wrote the initial version of the manuscript. MH, ML, SW, JO, and FK commented on the initial  
475 manuscript and helped improve it. SB developed the methodology with inputs from MH. SB performed the  
476 analysis with support from MH and ML. SB and MH participated in the fieldwork.

## FUNDING

477 This work was supported and funded by the University of Fribourg and by the Swiss Government Excellence  
478 Scholarship (SB).

## ACKNOWLEDGMENTS

479 We thank Mr. Adolf Kaeser and Mr. Flavio Catillaz at Eispalast Schwarzsee for their active participation  
480 in the fieldwork. We would also like to thank Digmesa AG for subsidising their flowmeter used in the  
481 experiment. We would particularly like to thank the editor Prof. Thomas Schuler and 2 anonymous  
482 reviewers who gave us important inputs to improve the paper. We also thank Prof. Christian Hauck, Prof.  
483 Nanna B. Karlsson and Dr. Andrew Tedstone for valuable suggestions that improved the manuscript.

## DATA AVAILABILITY STATEMENT

484 The data and code used to produce results and figures will be published at a later stage and can, until then,  
485 be obtained from the authors upon request.

## REFERENCES

- 486 Apel, H., Abdykerimova, Z., Agalhanova, M., Baimaganbetov, A., Gavrilenko, N., Gerlitz, L., et al. (2018).  
487 Statistical forecast of seasonal discharge in central asia using observational records: development of a  
488 generic linear modelling tool for operational water resource management. *Hydrology and Earth System  
489 Sciences* 22, 2225–2254. doi:10.5194/hess-22-2225-2018
- 490 Bonales, L. J., Rodriguez, A. C., and Sanz, P. D. (2017). Thermal conductivity of ice prepared under  
491 different conditions. *International Journal of Food Properties* 20, 610–619. doi:10.1080/10942912.  
492 2017.1306551
- 493 Buck, A. L. (1981). New equations for computing vapor pressure and enhancement factor. *Journal of  
494 Applied Meteorology and Climatology* 20, 1527 – 1532
- 495 Buytaert, W., Moulds, S., Acosta, L., Bievre, B. D., Olmos, C., Villacis, M., et al. (2017). Glacial melt  
496 content of water use in the tropical andes. *Environmental Research Letters* 12, 114014. doi:10.1088/  
497 1748-9326/aa926c
- 498 Chen, Y., Li, W., Deng, H., Fang, G., and Li, Z. (2016). Changes in central asia's water tower: Past, present  
499 and future. *Nature* doi:10.1088/1748-9326/aa926c
- 500 Chevuturi, A., Dimri, A. P., and Thayyen, R. J. (2018). Climate change over leh (ladakh), india. *Theoretical  
501 and Applied Climatology* 131, 531–545. doi:10.1007/s00704-016-1989-1
- 502 [Dataset] Copernicus Climate Change Service (C3S) (2017). Era5: Fifth generation of ecmwf atmospheric  
503 reanalyses of the global climate. [Available at [https://cds.climate.copernicus.eu/  
504 cdsapp#!/home](https://cds.climate.copernicus.eu/cdsapp#!/home), accessed 2019-10-01]
- 505 Cuffey, K. M. and Paterson, W. S. B. (2010). *The Physics Of Glaciers* (Elsevier)

- 506 Fujita, K. and Ageta, Y. (2000). Effect of summer accumulation on glacier mass balance on the  
507 tibetan plateau revealed by mass-balance model. *Journal of Glaciology* 46, 244–252. doi:10.3189/172756500781832945
- 509 Fujita, K., Hiyama, K., Iida, H., and Ageta, Y. (2010). Self-regulated fluctuations in the ablation of a snow  
510 patch over four decades. *Water Resources Research* 46, W11541. doi:10.1029/2009WR008383
- 511 Garratt, J. R. (1992). *The Atmospheric Boundary Layer* (Cambridge University Press)
- 512 Grossman, D. (2015). As himalayan glaciers melt, two towns face the fallout [Available at  
513 [https://e360.yale.edu/features/as\\_himalayan\\_glaciers\\_melt\\_two\\_towns\\_](https://e360.yale.edu/features/as_himalayan_glaciers_melt_two_towns_face_the_fallout)  
514 [face\\_the\\_fallout](https://e360.yale.edu/features/as_himalayan_glaciers_melt_two_towns_face_the_fallout), accessed 2019-10-01]
- 515 Hock, R. (2005). Glacier melt: a review of processes and their modelling. *Progress in Physical Geography: Earth and Environment* 29, 362–391
- 517 Hock, R., Rasul, G., Adler, C., Cáceres, B., Gruber, S., Hirabayashi, Y., et al. (2019). 2019: High mountain  
518 areas. *IPCC Special Report on the Ocean and Cryosphere in a Changing Climate* [H.-O. Pörtner, D.C.  
519 Roberts, V. Masson-Delmotte, P. Zhai, M. Tignor, E. Poloczanska, K. Mintenbeck, A. Alegría, M. Nicolai,  
520 A. Okem, J. Petzold, B. Rama, N.M. Weyer (eds.)]
- 521 Hoelzle, M., Barandun, M., Bolch, T., Fiddes, J., Gafurov, A., Muccione, V., et al. (2019). *The status and role of the alpine cryosphere in Central Asia*. doi:10.4324/9780429436475-8
- 523 Hori, M., Aoki, T., Tanikawa, T., Motoyoshi, H., Hachikubo, A., Sugiura, K., et al. (2006). In-situ  
524 measured spectral directional emissivity of snow and ice in the 8–14 micrometer atmospheric window.  
525 *Remote Sensing of Environment* 100, 486 – 502
- 526 [Dataset] IDAWEB (2019). Meteoswiss, federal office of meteorology and climatology. [Available at  
527 <https://gate.meteoswiss.ch/idaweb/login.do>, accessed 2019-10-01]
- 528 Immerzeel, W. W., Lutz, A. F., Andrade, M., Bahl, A., Biemans, H., Bolch, T., et al. (2019). Importance  
529 and vulnerability of the world's water towers. *Nature* 577, 364 – 369. doi:10.1038/s41586-019-1822-y
- 530 Meteoblue (2020). Climate schwarzsee [Available at [https://www.meteoblue.com/en/weather/historyclimate/climatemodelled/schwarzsee\\_switzerland\\_11790334](https://www.meteoblue.com/en/weather/historyclimate/climatemodelled/schwarzsee_switzerland_11790334), accessed 2019-10-01]
- 533 Mölg, T. and Hardy, D. R. (2004). Ablation and associated energy balance of a horizontal glacier surface  
534 on kilimanjaro. *J. Geophys. Res.-Atmos.* 109, 1–13. doi:10.1029/2003JD004338
- 535 Nüsser, M., Dame, J., Kraus, B., Baghel, R., and Schmidt, S. (2019a). Socio-hydrology of artificial glaciers  
536 in ladakh, india: assessing adaptive strategies in a changing cryosphere. *Regional Environmental Change*  
537 doi:10.1007/s10113-018-1372-0
- 538 Nüsser, M., Dame, J., Parveen, S., Kraus, B., Baghel, R., and Schmidt, S. (2019b). Cryosphere-Fed  
539 Irrigation Networks in the Northwestern Himalaya: Precarious Livelihoods and Adaptation Strategies  
540 Under the Impact of Climate Change. *Mountain Research and Development* 39. doi:10.1659/MRD-JOURNAL-D-18-00072.1
- 542 Oerlemans, J. and Knap, W. H. (1998). A 1 year record of global radiation and albedo in the  
543 ablation zone of morteratschgletscher, switzerland. *Journal of Glaciology* 44, 231–238. doi:10.3189/S0022143000002574
- 545 Scherrer, S. C. (2020). Temperature monitoring in mountain regions using reanalyses: lessons from the  
546 alps. *Environmental Research Letters* 15, 044005
- 547 Schmidt, L. S., Aðalgeirs Þóttir, G., Guðmundsson, S., Langen, P. L., Pálsson, F., Mottram, R., et al. (2017).  
548 The importance of accurate glacier albedo for estimates of surface mass balance on vatnajökull: evaluating  
549 the surface energy budget in a regional climate model with automatic weather station observations. *The Cryosphere* 11, 1665–1684. doi:10.5194/tc-11-1665-2017

- 551 Stigter, E. E., Litt, M., Steiner, J. F., Bonekamp, P. N. J., Shea, J. M., Bierkens, M. F. P., et al. (2018).  
552 The importance of snow sublimation on a himalayan glacier. *Frontiers in Earth Science* 6, 108.  
553 doi:10.3389/feart.2018.00108
- 554 Tetens, O. (1930). Uber einige meteorologische begriffe. z. *Geophys.* 6, 297–309
- 555 Unger-Shayesteh, K., Vorogushyn, S., Farinotti, D., Gafurov, A., Duethmann, D., Mandychev, A., et al.  
556 (2013). What do we know about past changes in the water cycle of central asian headwaters? a review.  
557 *Global and Planetary Change* 110, 4 – 25. doi:10.1016/j.gloplacha.2013.02.004. Water in Central Asia  
558 – Perspectives under global change
- 559 Wangchuk, S. (2014). Ice stupa artificial glaciers of ladakh [Available at [www.indiegogo.com/projects/ice-stupa-artificial-glaciers-of-ladakh#/](http://www.indiegogo.com/projects/ice-stupa-artificial-glaciers-of-ladakh#/), accessed 2019-10-01]
- 560 Wangchuk, S. (2015a). The good news at ice stupa 24th january 2015 [Available at <http://icestupa.org/news/the-good-news-at-ice-stupa>, accessed 2019-10-01]
- 561 Wangchuk, S. (2015b). Ice stupa artificial glacier inaugurated  
562 5th of march 2015 [Available at <http://icestupa.org/news/ice-stupa-artificial-glacier-inaugurated-5th-of-march>,  
563 accessed 2019-10-01]
- 564 Wangchuk, S. (2015c). Ice stupa surpasses guiness world record [Available at <http://icestupa.org/news/ice-stupa-surpasses-guinness-world-record>, accessed 2019-10-01]
- 565 Wangchuk, S. (2015d). Ice stupa way of celebrating a special day [Available at <http://icestupa.org/news/ice-stupa-way-of-celebrating-a-special-day6th-of-ju>,  
566 accessed 2019-10-01]
- 567 Wangchuk, S. (2015e). World water day at ice stupa [Available at <http://icestupa.org/news/world-water-day-at-ice-stupa>, accessed 2019-10-01]
- 568 WMO (2018). *Guide to Instruments and Methods of Observation* (World Meteorological Organization ;  
569 2018 (2018 Edition))
- 570 Woolf, H. M. (1968). *On the Computation of Solar Elevation Angles and the determination of sunrise and*  
571 *sunset times* (National Aeronautics and Space Administration)
- 572 Zhou, S., Kang, S., Gao, T., and Zhang, G. (2010). Response of zhadang glacier runoff in nam co basin,  
573 tibet, to changes in air temperature and precipitation form. *Chinese Science Bulletin* 55, 2103–2110.  
574 doi:10.1007/s11434-010-3290-5